Acta Materialia 205 (2021) 116556

Contents lists available at ScienceDirect

Acta Materialia

journal homepage: www.elsevier.com/locate/actamat

Ductile damage of AA2024-T3 under shear loading: Mechanism analysis through in-situ laminography

Thomas Tancogne-Dejean[a], Christian C. Roth[a], Thilo F. Morgeneyer[b], Lukas Helfen[c,d], Dirk Mohr[a,*]

[a] Department of Mechanical and Process Engineering, ETH Zurich, Switzerland
[b] MINES ParisTech, PSL University, Centre des Matériaux, CNRS UMR 7633, Evry, France
[c] Institute for Photon Science and Synchrotron Radiation, KIT, Germany
[d] European Synchrotron Radiation Facility (ESRF), Grenoble, France

ARTICLE INFO

Article history:
Received 4 September 2020
Revised 2 December 2020
Accepted 6 December 2020
Available online 16 December 2020

Keywords:
In situ
Synchrotron radiation computed tomography
Aluminum alloy
Ductile fracture
Shear

ABSTRACT

The mechanisms leading to fracture of aluminum alloy AA2024-T3 under shear loading are investigated via X-ray synchrotron laminography. A 1mm-thick flat double-gage section shear specimen is loaded inside a synchrotron X-ray beamline. The microscale defects population is reconstructed on six loading steps as well as on the broken specimen. The material exhibits an initial void volume fraction of 0.7% as well as a high concentration of large Cu-rich intermetallic particles. Using 2D Digital Image Correlation of projected volume data, based on the void contrast, it is possible to track the evolution of both types of mesoscale defects throughout the loading and to correlate the deformation mechanisms with the local strains. Upon mechanical loading, pre-existing voids rotate and elongate following the deformation of the aluminum matrix. The intermetallic particles fail at early loading stages in a brittle manner, leading to the nucleation of voids normal to the maximum principal stress direction. The newly-created voids continue to grow during the subsequent loading steps impeded by the fragmented particles, eventually forming micro-cracks. A fracture mechanism is proposed based on these observations and assessed with a representative volume element simulation, pointing towards the formation of a shear localization band during the final loading step.

1. Introduction

After half a century of research on ductile fracture, it is widely accepted that void nucleation, growth and coalescence are the main mechanisms leading to the ductile fracture of polycrystalline metals (e.g. [1]). Ductile failure is a process in which plastic deformation promotes the progressive damage of solids all the way until fracture initiation. The seminal works of McClintock [2] and Rice and Tracey [3] showed the pronounced dependence of the ductile failure process on the stress state. For several decades, most research in the field focused on the important effect of the stress triaxiality, while it is only recently that the second variable characterizing the stress state, that is the Lode parameter, received also significant attention (e.g. [4–6]).

Phenomenological models have emerged that describe the dependence of ductile fracture on both the stress triaxiality and the Lode angle parameter (e.g. [7–10]). At the same time, advanced porous plasticity models have been developed (e.g. [11–14]) based on the mathematical description of the assumed micro- and/or meso-structural deformation mechanisms. In addition, attempts have been made to come up with an enhanced void nucleation rule that incorporates the dependence on the Lode parameter of the strain rate tensor [15]. Many studies focus on positive stress triaxialities (e.g. [16–19]), while only a limited number of publications address the damage mechanism under (simple) shear loading. For example, Fleck et al. [20] assessed numerically the effect of void nucleation from cylindrical particles in tension and shear. Torki et al. [21] developed a model based on homogenization that takes into account void coalescence in porous ductile solids. Numerical simulations demonstrated the closure of voids under shear loading [22] as well as the effect of the Lode parameter on plastic flow localization after proportional loading at low stress triaxialities [23]. Morin et al. [24] assessed the performance of the model derived by Madou and Leblond [13] for shear-

* Corresponding author.
E-mail address: mohr@mit.edu (D. Mohr).

https://doi.org/10.1016/j.actamat.2020.116556

dominated loading. Their results show that void shape changes can lead to softening in absence of void growth.

To experimentally investigate the effect of the stress state on material ductility, a variety of multiaxial testing campaigns has been developed (e.g. [25–28]). More recently, emphasis has been placed on developing experiments with proportional loading histories to minimize the effect of load path changes (e.g. [29]). The case of simple shear loading received particular attention, as obtaining fracture initiation in this stress state is challenging because of the risk of premature fracture from a free boundary subjected to uniaxial tension. Several specimen geometries have been proposed (e.g. [30–32]) with various cut-out shapes. Roth and Mohr [29] proposed a shape-optimization procedure, specifically tailoring the specimen geometry to the plastic properties of a material in order to obtain shear fracture. This methodology is also applied to the specimen design in the present work.

Only few experimental techniques allow for analyzing damage in real materials. Post mortem investigations comprising metallography and fractography have been used to assess the shape and number of particles and voids in single planes or across the fracture surface. Mohr and Treitler [33] analyzed the fracture mechanism in the pressure die casting alloy Al-10Si-Mg-Mn at different stress triaxialities. According to their metallographic observations, final fracture is always due to the linking of micro-cracks. In their material, particle cracking led to void nucleation and subsequent micro-crack formation at positive stress triaxialities, while particle debonding appeared to dominate at nearly zero stress triaxiality. Gross and Ravi-Chandar [34] performed shear experiments on aluminum 6061-T6 inside the chamber of a scanning electron microscope (SEM) to assess the evolution of particles at the sample surface. Papasidero et al. [35] monitored the damage evolution in aluminum 2024-T351 during in-situ torsion tests.

To overcome the limitations of SEM-based observations, X-ray micro-tomography techniques [36] and related synchrotron imaging methods [37] have been developed. A comprehensive review of (synchrotron) tomography applied to material science can be found in [38]. These in-situ volumetric observations at the sub-micrometer scale provide an unambiguous history of damage micro-mechanisms during loading. Synchrotron laminography has proven to be particularly suitable for investigating specific regions of interest in sheet metal (e.g. [15,39]). It is based on the acquisition of a series of radiographs of the region of interest (ROI) and the subsequent computer-aided reconstruction [40]. Leveraging this technique, Ueda et al. [41] could even monitor the evolution of individual voids during the ductile tearing of 1mm thick aluminum specimens. With the presence of "natural markers", i.e. second phase particles or voids, this technique allows for Digital Volume Correlation (DVC). In the absence of through thickness strain gradients, planar digital image correlation based on projected slices provides a viable alternative [42]. Using DVC, Buljac et al. [43] detected bands of localized deformation in a compact tension specimen already at the early stage of loading.

In the present work, the mechanisms resulting in ductile fracture under simple shear are examined using X-ray laminography in an aluminum alloy AA2024-T3. Images are acquired at six different stages throughout the shear fracture experiment as well as after specimen failure. Projection DIC is employed extensively to analyze the strain field and track individual voids through the loading steps. The evolution of the void volume and the number of voids is presented for quantitative analysis. At the same time, the spatial distribution of the void shape and volume are analyzed with respect to the effective strain over selected line profiles. A fracture mechanism is postulated and discussed based on fractography observations and the results from a numerical study with a representative volume element (RVE).

Table 1
Geometry parameters for the smiley shear specimens for AA2024. All dimensions are given in mm as denoted in [29].

[mm]	x_c	Δx	h	w	R_n,	Δx_n	R_f
AA2024	2.986	0.136	1.202	1.501	0.233	0.000	1.608

2. Methods

2.1. Experimental techniques

2.1.1. Specimen geometry

The specimen geometry follows the design of a "smiley" shear specimen as introduced by Roth and Mohr [29]. The specimen features two parallel gauge sections to induce shear-dominated loading up to fracture on a sheet metal specimen using a uniaxial tensile actuator. The design of the cutouts is obtained from a shape optimization framework which aims at delaying fracture from the free boundaries of the gauge section. The specimen also reduces the occurrence of through-thickness strain and stress gradients. Details of the geometry can be found in [29], with Table 1 presenting the dimensions of the specimen used. The specimen is directly extracted from the sheet material through wire electric discharge machining.

2.1.2. Material

The study investigates the damage mechanisms in an AA2024-T3 aluminum alloy provided as 1 mm thick sheet. In view of Electron Back-Scattered Diffraction (EBSD) analysis, a specimen is prepared through mechanical grinding up to a SiC paper with grit of 4000, followed by polishing with a diamond suspension and finished using a silica colloid with a grain size of 100nm. EBSD is performed in a scanning electron microscope (Scios, FEI) with a step size of $0.5\mu m$ and an acceleration voltage of 20kV. The material features a grain size from $15\mu m$ up to $60\mu m$ (see Fig. 2). The grain size distribution is heterogeneous with clusters of small grains and large crystals. The microstructure is also characterized by the presence of two classes of intermetallic particles: Al–Cu–Fe–Mn(–Si) and Al–Cu–Mg with a size of up to $50\mu m$ as revealed by the EBSD and laminography images. Furthermore, micron-sized intermetallic particles are also visible on the laminography reconstruction.

2.1.3. Fractography

Images of the fracture surface are acquired using a FEG SEM (Gemini, Zeiss) with an acceleration voltage of $10kV$. To enhance the contrast between the matrix and the second phase particles, the back-scattered electron detector is used. The matrix appears as dark grey while the particles are shown in lighter grey.

2.1.4. Laminography and image reconstruction

The laminography experiment is performed at the imaging beamline ID19 of the European Synchrotron Radiation Facility (ESRF, Grenoble, France). The laminography rotation axis is inclined with respect to the X-ray beam direction by an angle of about 65° (standard parallel-beam tomography would correspond to 90°). Displacement controlled, symmetric and monotonic stepwise loading via a dedicated electromechanical loading device is performed at $30\mu m/min$. The force is measured by an attached 5kN load cell (ME-Meßsysteme KD40s). The details of the setup are shown in Fig. 3. The scanning region is positioned between the roots of the two notches on one side of the sample (blue marked area see Fig. 1). Six loading steps are applied prior to fracture with the corresponding force levels: ①-300N, ②-600N, ③-700N, ④-790N, ⑤-865N and ⑥-920N (Fig. 7). A final scan ⑦ is performed on the broken specimen.

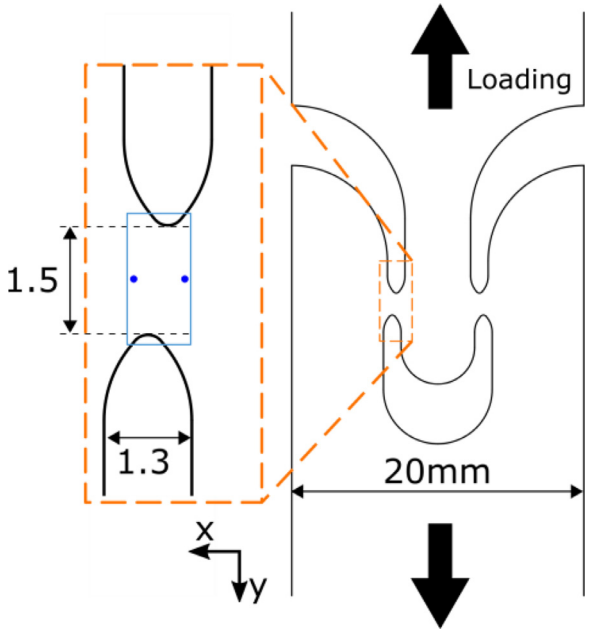

Fig. 1. Sketch of the specimen with highlighted area of interest (light blue square). The dark blue dots denotes the position of the extensometer used to measure the displacement of the gauge section. (For interpretation of the references to color in this figure legend, the reader is referred to the web version of this article.)

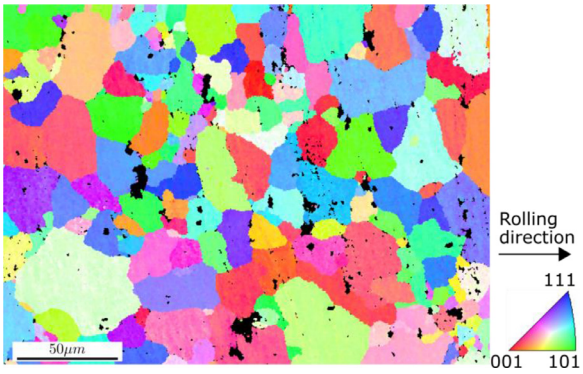

Fig. 2. Inverse pole figure of the AA2024-T3. The black zones show intermetallic particles that are not indexed during the analysis.

A pink beam from a single-line undulator with a 13 mm period (using a configuration with the so-called deflection parameter K<1 ([44]) filtered with 5.6 mm Al and a peak X-ray energy around 26 keV is chosen, as it allows for a good compromise between X-ray transmission / penetration power and image contrast [45]. For a full scan, a series of 3,599 radiographs is acquired. During this process, the sample mounted in the tensile machine is rotated by 360° on the laminography rotation stage, corresponding to a rotation of approx. 0.1° per angular step. An exposure time of 50 ms per radiograph is chosen. The radiographs are then processed to reconstruct 3D volumes by using a filtered-back projection algorithm [46]. The parameter optimization is performed automatically using a GPU-accelerated implementation of this algorithm [47]. The reconstructed volume is represented by a discrete grey level field (8-bit deep). It has a size of $2560 \times 2560 \times 2300$ voxels. The physical size (length) of one cubic voxel is equal to 0.65 µm. Each voxel inside the reconstructed volume contains the grey level related to the attenuation coefficient for X-rays. In the present case, the image contrast is mainly due to heavy intermetallic particles of some micrometers size and preexisting voids.

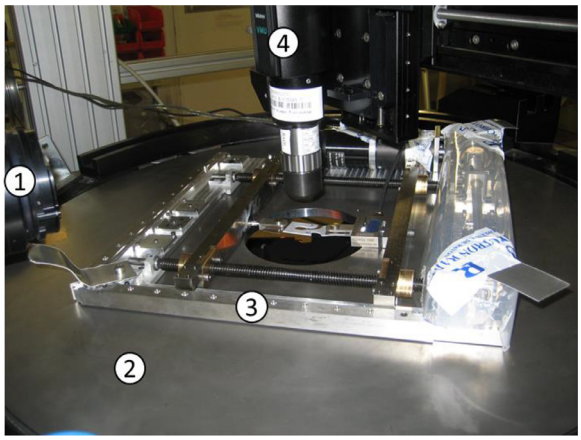

(a)

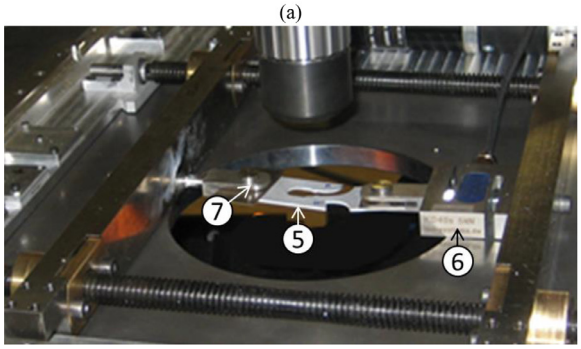

(b)

Fig. 3. Experimental setup showing ① X-ray detector, ② Rotating laminography platform, ③ Electro-mechanical in situ tensile machine, ④ Optical microscope, ⑤ Shear specimen (broken), ⑥ 5 kN Load cell and ⑦ Loading pin.

2.1.5. Image processing methods

The reconstructed images are further cropped to center on the gauge section, resulting in a final volume size of $1400 \times 2560 \times 1000$ voxels, corresponding to a $650\mu m$ thick slice around the mid-plane of the specimen. The laminography images are used in two different ways: (i) to investigate the evolution of the void and particle populations and (ii) to perform Digital Image Correlation (DIC) to assess the local strain fields inside the material.

In order to characterize the evolution of the void population, segmentation via a global region growing algorithm is used to separate the voids from the bulk of the material. The seeds correspond to voxels with a grey level below 40 (out of 256) and the growth continues with surrounding voxels of grey levels up to 80. For the last step, due to the different scanning conditions, the seed and growth values are set to 80 and 100 respectively. A similar procedure has been applied in [48]. It should be noted here that both values are chosen as a compromise between the laminography's artifacts, such as edge contrast around particles and the features of interest, i.e. voids. Finally, morphological operations are applied to close the small pores while preserving the shape of the large voids. To account for errors and artifacts of the laminography technique, the minimum void volume to be considered is chosen as $3 \times 3 \times 3$ voxels, corresponding to a physical volume of $7.41\mu m^3$. It is challenging to assess the uncertainties introduced by the described segmentation as they originate from a long chain of data acquisition, reconstruction and treatment with the segmentation as the final step. Following the work of Trejo-Navas et al. [49] the uncertainties in the void volume fraction can be estimated to be up to 10%. Similar uncertainties are expected to hold true for the number of voids in our work.

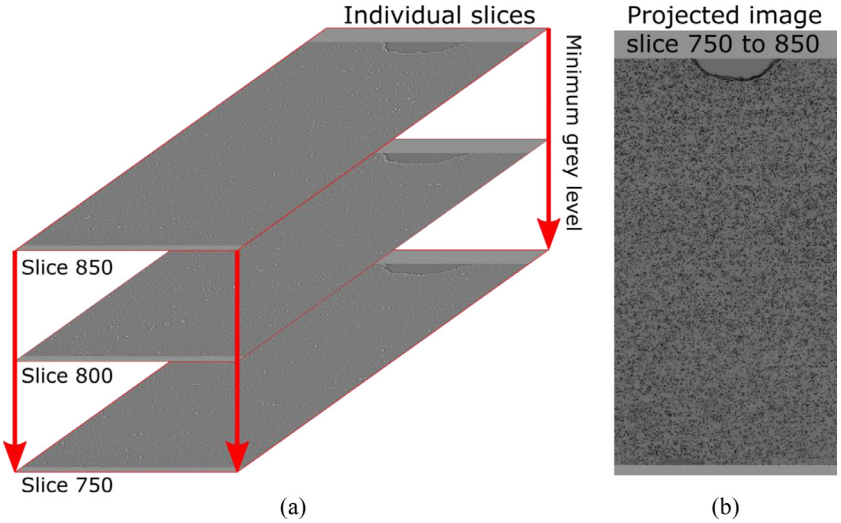

Fig. 4. Projection DIC with (a) the individual slices combined over $65\mu m$ and (b) the final image with the minimum grey level.

The volume of each void is extracted along with the principal axis length of the corresponding ellipsoid featuring the same second moment of inertia [50]. Based on the principal axes length, the Feret's shape factor is then introduced as the ratio of the minimum over the maximum principal axis length. This metric allows spherical and ellipsoidal voids to be distinguished. For a sphere the ratio reaches unity, while it decreases towards zero as the ellipsoid becomes a more two-dimensional object, which could be either needle- or disk-shaped.

2.1.6. DIC of projected 3D laminography data

The raw laminography images are also used to obtain the strain field in the gauge section. In view of the very small through-thickness strain gradient, it is possible to use two-dimensional projection DIC to obtain the strain field as presented in [42] and validated by comparison with DVC data in [43]. To increase the natural contrast given by the presence of voids and intermetallic particles, the minimum grey level (i.e. mostly voids) over 100 slices of 3D data (i.e. $65\mu m$) is projected to generate a 2D image for further DIC using the commercial software VIC-2D (Correlated Solution, USA). After confirming the minimal through-thickness gradients and the repeatability of the results with strain fields extracted from various locations on the specimen thickness, the through-thickness position of $Z = 520\mu m$, corresponding to slice 800 (see Fig. 4) is chosen as the representative position and used as mid-plane for the projection of the slices. The subset size is chosen as 69 pixels (i.e. $45\mu m$) with a step size of 15 pixels and a filter size of 5. Along with the strain field, the local displacement of the specimen is extracted based on a 0.8mm long-extensometer (blue dots on Fig. 1).

Using the DIC displacement field, it is possible to track the same volume during the deformation process and investigate the changes in the local defects population. The investigation is performed on different regions of the specimen. Three large vertical regions (Fig. 5: "Left", "Center", "Right") are selected, which separate the width of the sample into three equal zones of volume $275 \times 1500 \times 650\mu m$. In addition, three horizontal line profiles are selected on the top, middle and bottom of the gauge section (Fig. 5: solid cyan, magenta and green lines), each featuring a height of $200\mu m$. Each of the horizontal bands is then divided into 15 sub-regions, each with an average volume of $55 \times 200 \times 650\mu m$. As a strain measure for direct evaluation and comparison, the effective strain is introduced, defined as the von Mises equivalent strain assuming plastic incompressibility:

$$\varepsilon_{eff} = \frac{2}{\sqrt{3}}\sqrt{\varepsilon_I{}^2 + \varepsilon_{II}{}^2 + \varepsilon_I\varepsilon_{II}} \tag{1}$$

with ε_I and ε_{II} denoting the maximum and minimum in-plane principal strains [29].

2.2. Numerical techniques

In order to better assess the stress and strain state inside the gauge section, a numerical simulation of the shear test is carried out.

2.2.1. Finite element model

Closely following [29], only a quarter of the specimen with half of the geometry's thickness is modeled thereby exploiting all symmetries. To accurately represent any deformation, a very fine mesh size of approximately $l_e = 25\mu m$ is chosen in the gauge section where the largest plastic deformation occurs. This results in 143'300 out of the 193'060 C3D8R reduced integration brick elements being located in this area (see Fig. 1 blue box). The finite element software Abaqus/Explicit (2016) is used to perform the numerical simulations. The lower boundary of the specimen is clamped, while a constant vertical velocity is applied to the upper boundary. Uniform mass scaling is applied in the quasi-static simulation, so that the simulation terminates after approximately 680,000 time steps.

2.2.2. Yield function and flow rule

To facilitate finite element simulations of the shear experiment, an extension of the Yld2000-2D constitutive model [51] to three dimensions is used, as also shown in [52] and [53]. The yield condition is defined by

$$f[\boldsymbol{\sigma}, k] = \bar{\sigma}_{Yld2000} - k = 0 \tag{2}$$

with the anisotropic equivalent stress $\bar{\sigma}_{Yld2000}$ and the deformation resistance k. The effect of material anisotropy is completely incorporated into the anisotropic equivalent stress definition under the assumption of associated plastic flow,

$$\bar{\sigma}_{Yld2000} = \frac{1}{\sqrt[m]{2}}(\phi'[\mathbf{s}'] + \phi''[\mathbf{s}''])^{1/m} \tag{3}$$

with the transformed stress deviators $\mathbf{s}' = [s'_{11}\, s'_{22}\, s'_{12}\, s'_{23}\, s'_{13}]^T$, $\mathbf{s}'' = [s''_{11}\, s''_{22}\, s''_{12}\, s''_{23}\, s''_{13}]^T$ and Hosford exponent m. Depending

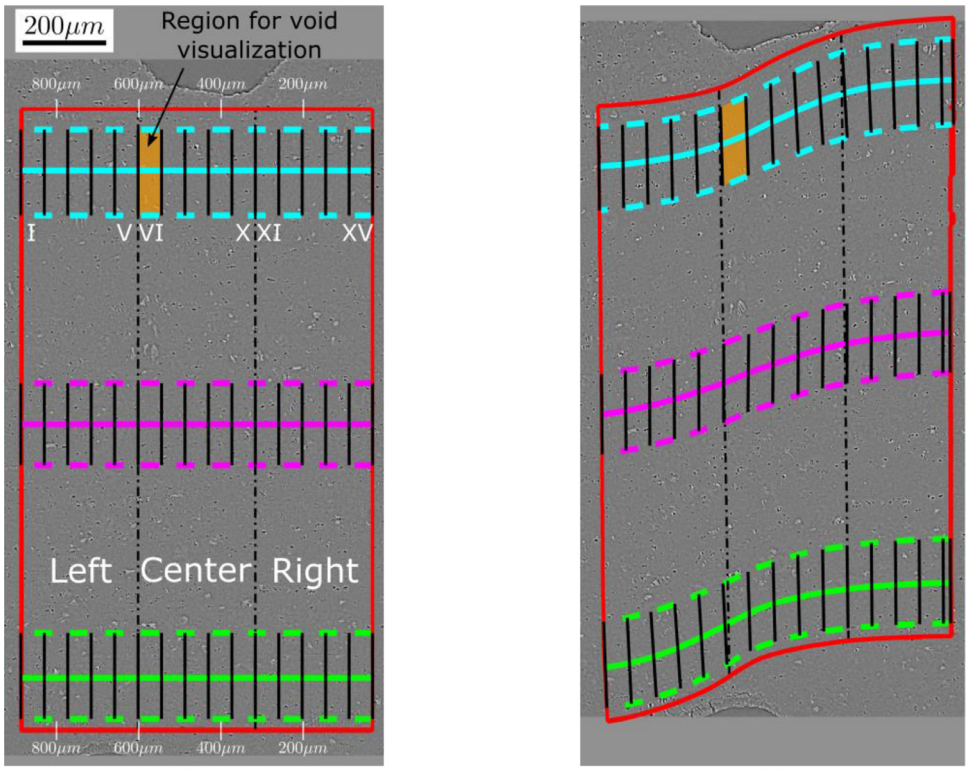

Fig. 5. Overview of the different zones used throughout the study (a) at the first step of loading ① (b) and at 920N ⑥. Three large regions ("Left", "Center", "Right"), 15 sub-regions along each of the three horizontal lines top (cyan), middle (magenta) and bottom (green) and an orange sub-region used for void visualization on Fig. 11. (For interpretation of the references to color in this figure legend, the reader is referred to the web version of this article.)

on the same $\alpha_1, \ldots, \alpha_8$ as the original Yld2000-2D, the two linear transformations $\mathbf{s}' = \mathbf{L}'\sigma$ and $\mathbf{s}'' = \mathbf{L}''\sigma$ are defined through two tensors:

$$\mathbf{L}' = \frac{1}{3}\begin{bmatrix} 2\alpha_1 & -\alpha_1 & -\alpha_1 & 0 & 0 & 0 \\ -\alpha_2 & 2\alpha_2 & -\alpha_2 & 0 & 0 & 0 \\ 0 & 0 & 0 & 3\alpha_7 & 0 & 0 \\ 0 & 0 & 0 & 0 & 3 & 0 \\ 0 & 0 & 0 & 0 & 0 & 3 \end{bmatrix} \tag{4}$$

$$\mathbf{L}'' = \frac{1}{9}\begin{bmatrix} -2\alpha_3 + 2\alpha_4 + 8\alpha_5 - 2\alpha_6 & -4\alpha_4 + 4\alpha_6 + \alpha_3 - 4\alpha_5 & \alpha_3 + 2\alpha_4 - 4\alpha_5 - 2\alpha_6 & 0 & 0 & 0 \\ 4\alpha_3 - 4\alpha_4 - 4\alpha_5 + \alpha_6 & -2\alpha_3 + 8\alpha_4 + 2\alpha_5 - 2\alpha_6 & -2\alpha_3 - 4\alpha_4 + 2\alpha_5 + \alpha_6 & 0 & 0 & 0 \\ 0 & 0 & 0 & 9\alpha_8 & 0 & 0 \\ 0 & 0 & 0 & 0 & 9 & 0 \\ 0 & 0 & 0 & 0 & 0 & 9 \end{bmatrix} \tag{5}$$

The functions $\phi'[\mathbf{s}']$ and $\phi''[\mathbf{s}'']$ are used for the extension of the Yld2000-2D to three dimensions:

$$\phi'\left[s'\right] = \left[\left(s'_{11} - s'_{22}\right)^2 + 4\left(s'^2_{12} + s'^2_{23} + s'^2_{13}\right)^2\right]^{m/2} \tag{6}$$

$$\phi''[\mathbf{s}''] = \left[\frac{3}{2}\left(s''_{11} + s''_{22}\right)^2 + \frac{1}{2}\sqrt{\left(s''_{11} - s''_{22}\right)^2 + 4\left(s''^2_{12} + s''^2_{23} + s''^2_{13}\right)^2}\right]^m + \left[\frac{3}{2}\left(s''_{11} + s''_{22}\right)^2 - \frac{1}{2}\sqrt{\left(s''_{11} - s''_{22}\right)^2 + 4\left(s''^2_{12} + s''^2_{23} + s''^2_{13}\right)^2}\right]^m \tag{7}$$

For the particular case of plane stress, the function reduces to the Yld2000-2D, which for the specific case of $\alpha_1, \ldots, \alpha_8 = 1$ and $m = 2$ reduces to the von Mises yield criterion. Fig. 6 shows the yield surface of the calibrated YLD2000 model together with a von Mises yield surface (solid orange line) as reference. The parameters of the plasticity model for the AA2024-T3 are given in Table 2 and the calibration procedure is shown in [54].

2.2.3. Isotropic hardening law

The relationship between the deformation resistance k and the work-conjugate equivalent plastic strain $\bar{\varepsilon}_p$ is established by an isotropic hardening law,

$$k = k[\bar{\varepsilon}_p] \tag{8}$$

Based on the results of [54] a linear combination of a power law [55]

$$k_S[\bar{\varepsilon}_p] = A(\bar{\varepsilon}_p + \varepsilon_0)^n \tag{9}$$

and an exponential law [56]

$$k_V[\bar{\varepsilon}_p] = k_0 + Q\left(1 - e^{-\beta\bar{\varepsilon}_p}\right) \tag{10}$$

are used to parametrize the hardening curve,

$$k[\bar{\varepsilon}_p] = \alpha_{SV}k_S[\bar{\varepsilon}_p] + (1 - \alpha_{SV})k_V[\bar{\varepsilon}_p] \tag{11}$$

with the weighting parameter $\alpha_{SV} \in [0, 1]$. In sum, the hardening law features seven parameters: the Swift parameters $\{A, \varepsilon_0, n\}$, the Voce parameters $\{k_0, Q, \beta\}$, and the weighting parameter α_{SV} which are given in Table 2.

Table 2
Identified material model parameters (Yld2000-3D) for aluminum 2024-T351.

E [GPa]	ν [−]	ρ [kg/m^3]					
70	0.33	2897					
α_1 [−]	α_2 [−]	α_3 [−]	α_4 [−]	α_5 [−]	α_6 [−]	α_7 [−]	α_8 [−]
0.91238	1.01375	1.00793	1.04601	0.98950	0.84111	1.03850	1.13875
A [MPa]	ε_0 [−]	n [−]	k_0 [MPa]	Q [MPa]	β [−]	α_{SV} [−]	
798.56	0.0178	0.202	363.84	240.03	10.533	0.368	

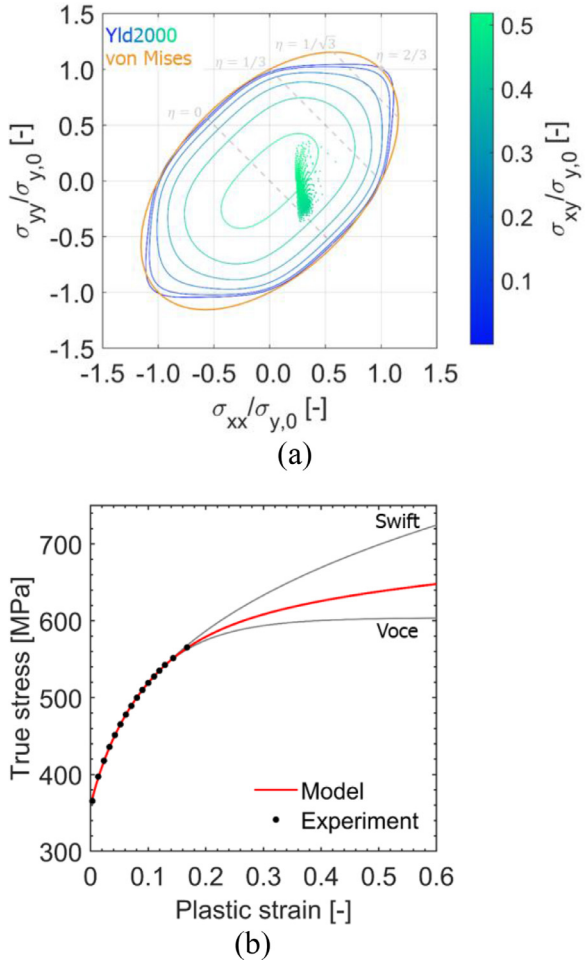

Fig. 6. Experimental and numerical results used for AA2024-T351: (a) Yield surface of the calibrated Yld2000-3D model. Solid dots represent the loading state as observed on the shear section mid-plane before fracture (step ⑥-920N). The von Mises yield surface is shown as reference in orange. (b) True stress - plastic strain response for uniaxial loading (black dots) and calibrated Swift-Voce strain hardening. (For interpretation of the references to color in this figure legend, the reader is referred to the web version of this article.)

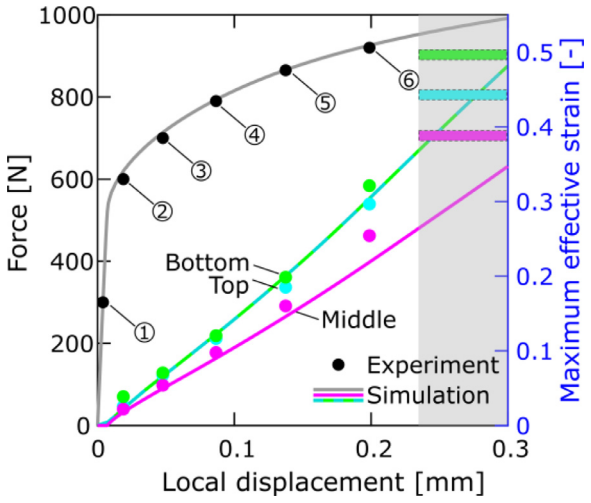

Fig. 7. Comparison of results from the experiment (dots) and numerical simulations (solid lines): Experimental force-displacement history (black) and comparison with the numerical simulation (grey). Effective strain values extracted from the specimen's top (cyan), middle (magenta) and bottom (green) area are shown on the secondary y-axis. The grey zone to the right indicates the uncertainty in the instant of fracture in the experiment. (For interpretation of the references to color in this figure legend, the reader is referred to the web version of this article.)

3. Results

3.1. Observations at the macroscopic level

Fig. 7 presents the evolution of the force against the local displacement of the specimen in six loading steps. The first loading step ① at 300N lies well within the elastic range of the experiment, while the second step (②-600N) is taken short after the onset of plastic deformation in the specimen. The subsequent steps show a significant increase in force in the plastic regime from 600N to 920N (⑥). Due to the unstable rupture in combination with the applied in situ load increments, the actual fracture displacement could not be obtained. This uncertainty is highlighted by a grey zone in Fig. 7.

Fig. 8 presents the evolution of the effective strain field on the specimen gauge section measured by projection DIC. Throughout the test, a localization of the deformation is observed. In between the two cutouts, two highly-strained regions form near the free top and bottom surface edges, i.e. close to the notches, while towards the middle of the gauge section the strain levels decrease slightly (~20%). The results obtained from DIC are further analyzed in Fig. 9. The effective strain field at step ⑥, right before fracture, is shown in Fig. 9a, while the line profiles for the top, middle and bottom are shown in Fig. 9b. The highest effective strain in the gauge section is measured on the bottom line with a value of 0.32, compared to 0.297 and 0.25 on the top and middle line, respectively. To gather a deeper insight in the strain state of the test, the ratio of the minimum to the maximum principal strain is calculated for the three line profiles at loading step ⑥ (Fig. 9c). For shear loading, this principal strain ratio equals to -1, while uniaxial tension and uniaxial compression result in values of -0.5 and -2, respectively. In the central region, between 400μm and 700μm, the principal strain ratio is between -0.9 and -1.1. However, due to the specimen geometry, the principal strain ratio changes towards the flanks of the gauge section, as discussed in detail in [57]. The significant noise in the principal strain ratio observed on the flanks is due to the low strain levels at these locations.

An overview of the evolution of the maximum effective strain along the three lines (top, middle and bottom) at each step is reported in Fig. 7. As expected from symmetry, the bottom and top maxima exhibit a very similar evolution. On the broken specimen ⑦, the bottom line exhibits a maximum effective strain of 0.50 on the fractured edge, while it reaches 0.45 and 0.4 on the top and middle line, respectively. Even though this measurement is taken

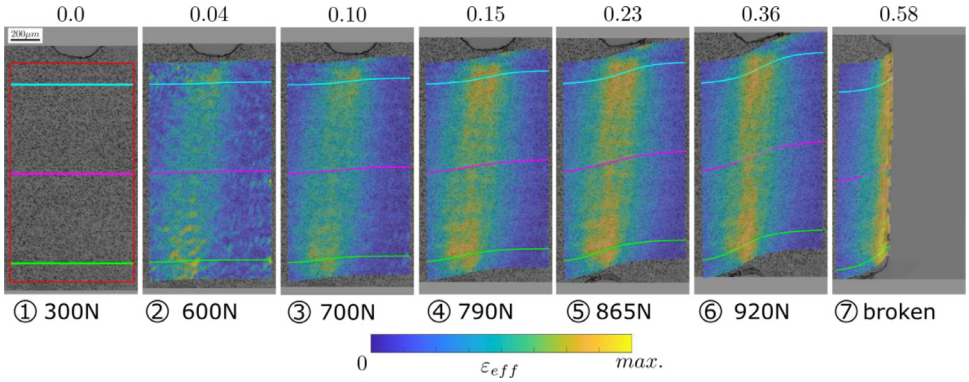

Fig. 8. Effective strain field evolution during the loading history measured by projection DIC at mid-sample thickness. The maximum effective strain is given on top of each load increment..

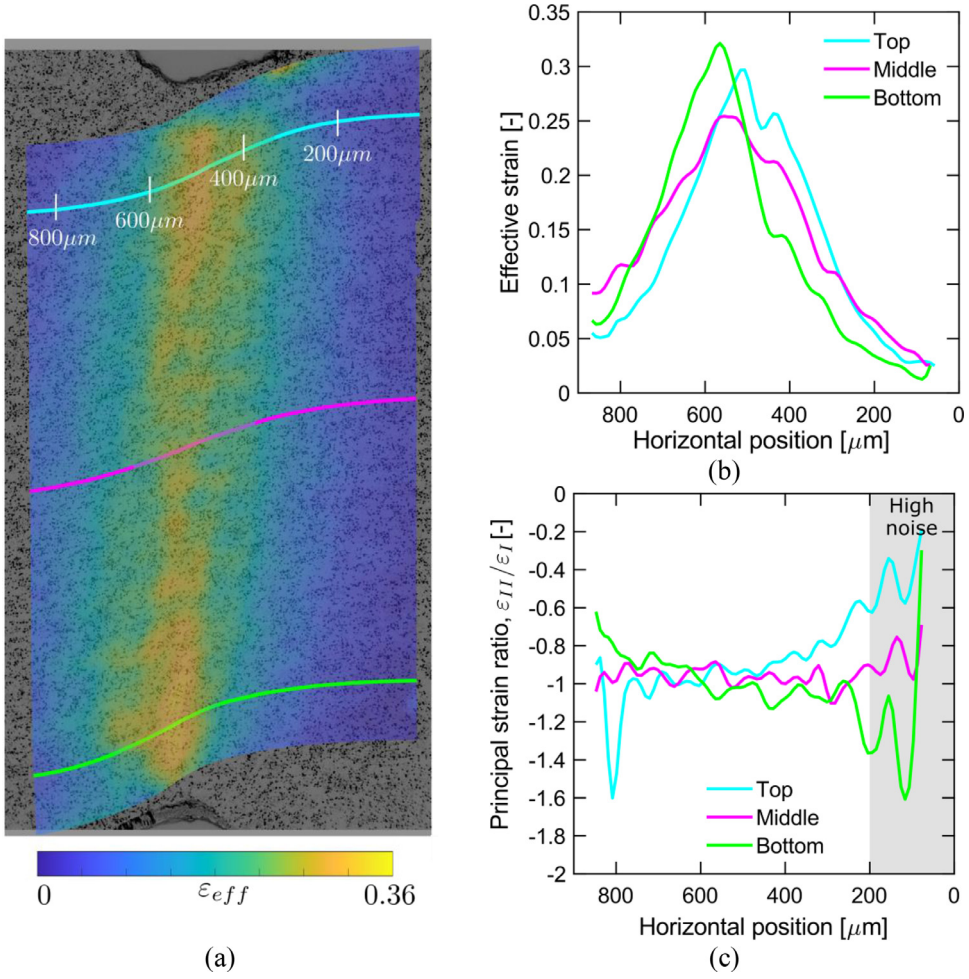

Fig. 9. Projection DIC strain field at step ⑥ (920N) right before onset of fracture. (a) Effective strain field highlighting the three lines at the top (cyan), middle (magenta) and bottom (green) of the gauge section. Line profiles of the effective strain (b) and the principal strain ratio (c) showing the loading state throughout the specimen. (For interpretation of the references to color in this figure legend, the reader is referred to the web version of this article.)

after elastic unloading and the crack might have not propagated along a line of maximum strain, this is an indicator that an acceleration of the deformation occurred towards the initiation of fracture, i.e. this points towards the presence of a shear localization band.

3.2. Observations at the microscopic level

To further exploit the laminography results and to gain insight into the damage micro mechanisms under shear, an investigation at the microscopic level is carried out. Fig. 10b,c show the evolution of representative key features in close-ups as denoted in Fig. 10a. The bounding boxes of the displacement field, as obtained from the projection DIC, are shown as references denoted by a solid line and can be used to estimate the deformation of the different zones (the exact strain values are provided by the full field in Fig. 8). The defects population consists of small and large intermetallic particles (Fig. 10b, light grey contrast) as well as voids (Fig. 10c, dark grey) which can also be seen in Fig. 5. The initial void volume fraction is computed from the laminography re-

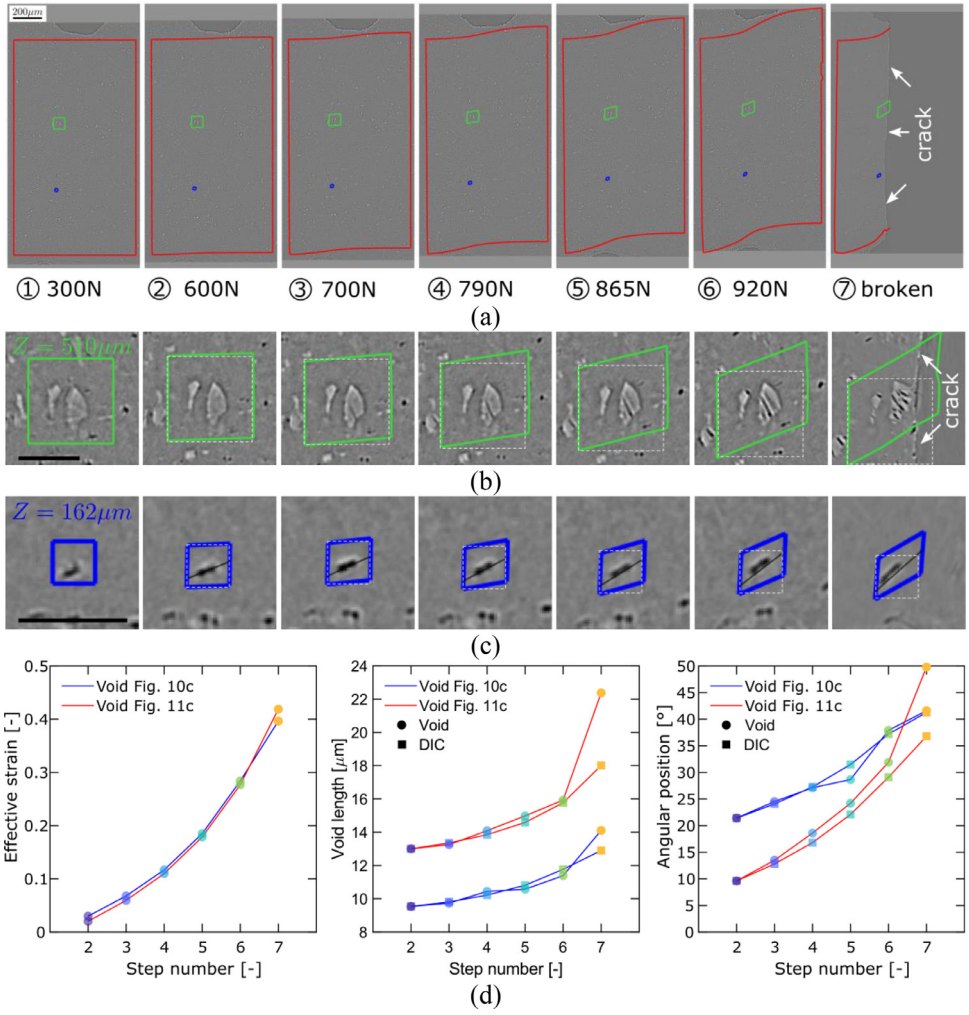

Fig. 10. (a). Deformation history of a slice located at 510μm with close-up view of (b) a large intermetallic and (c) an initial void. The black scale bars corresponds to 50 μm. The colored lines indicate the DIC contour while the black line denotes the rotation of the matrix according to DIC. (d) Evolution of the effective strain, the void length and the orientation for two selected voids. (For interpretation of the references to color in this figure legend, the reader is referred to the web version of this article.)

construction of step ② (600N) over the entire gauge section and reaches 0.007.

A large intermetallic particle, one of the two main microscopic features of the material, breaks multiple times during the deformation process (Fig. 10b). An initial crack is observed at step ③, which grows slowly until a second crack is observed at step ⑥, just before the particle shatters into 6 pieces during the final failure of the specimen (⑦). The initial crack normal appears at about 30° from the horizontal axis, which is kept almost constant until final failure after which an angle of 37° is measured. The DIC indicates that the effective strain value around these intermetallic particles increases from $[0.02, 0.05, 0.10, 0.16, 0.25, 0.35]$ during all loading steps. The maximum principal strain orientation is around 34° from the horizontal axis, which points towards the fact that the fracture plane is normal to the maximum tensile direction, which should correspond to the direction of maximum principal stress.

The pre-existing void (Fig. 10c) is initially oriented at 21.4° from the horizontal axis. Two measures are introduced to assess its evolution: (i) the maximum in-plane length and (ii) the angular position. Upon loading, the void elongates and rotates with the tendency to close as observed in the last step. This evolution is compared with results from DIC measurements of a bounding box in Fig. 10d. The bounding box (blue) and a line element with the same initial orientation (black) are added to Fig. 10c for visualization purposes The good agreement of the two measures partially validates the approach used in the subsequent sections, in which local void measurements, i.e. volume, principal axes and moments of inertia are used to assess the deformation behavior. Note that the slight difference in the orientation in step ⑤ is attributed to a laminography artefact.

3.3. Void and particle tracking

A sub-region (VI) located on the top line in the gauge section closest to the edge at final fracture is chosen to visualize the behavior of the voids (Fig. 5, orange box). Fig. 11 presents the evolution of the voids in the selected sub-region in three dimensions and confirms the settings chosen for the thresholding. Using the two-dimensional displacement field from the projection DIC and exploiting the negligible through-thickness strain, the voids are shown for all seven steps in the sub-region's reference configuration. To separate pre-existing from newly formed voids, from the initial to the last step all voids with centroids lying within a sphere of 5μm radius are considered identical.

All pre-existing voids are shown in grey while newly created voids are denoted in the color of the step they occur in. For the slice from 350μm to 550μm, initially there are 455 voids visible,

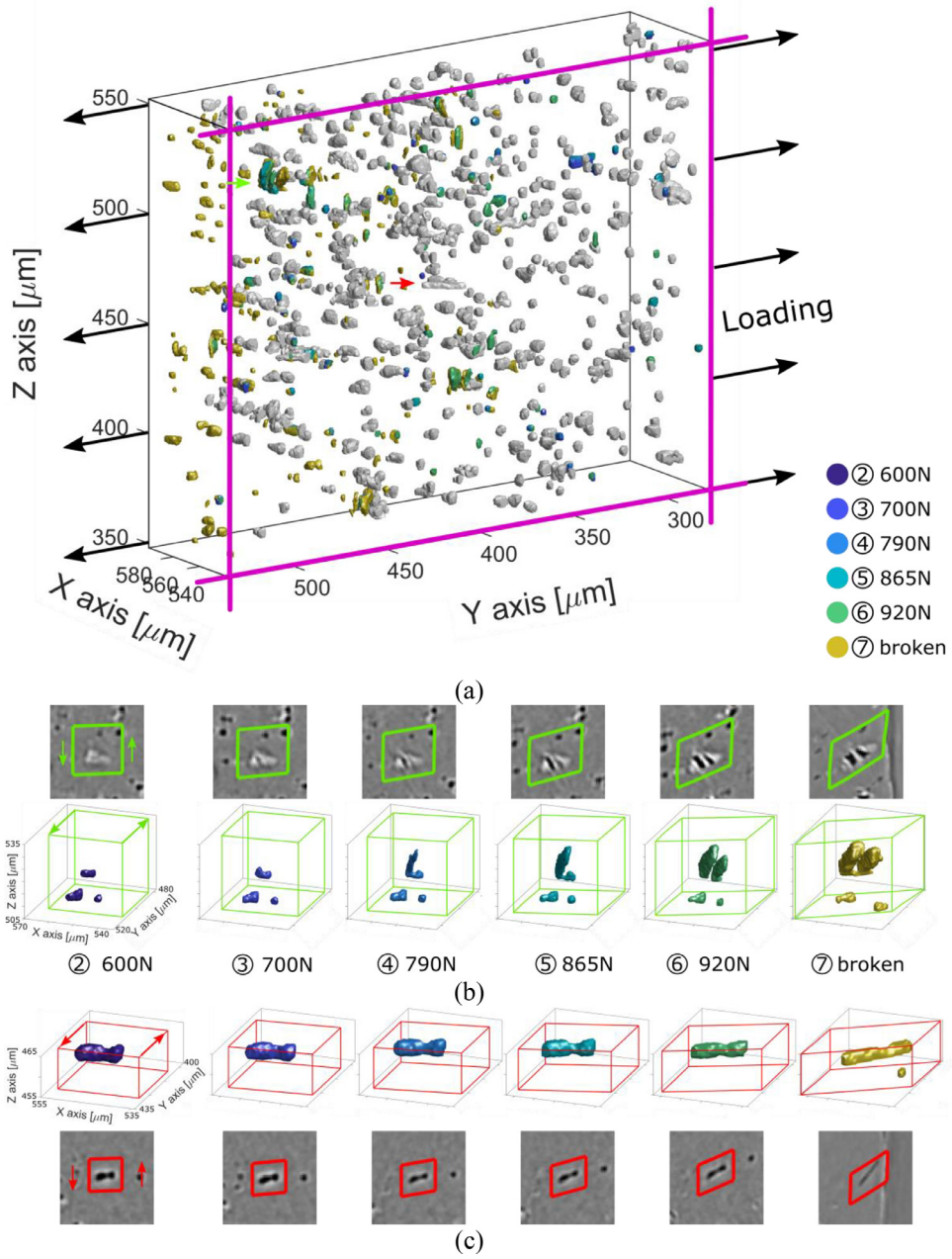

Fig. 11. Void evolution in the reference configuration for bin VI from Fig. 5. Pre-existing voids are shown in grey, while newly created voids are shown in the color of the respective step. The fracture plane is highlighted with the purple lines. (b) Close-up view on an intermetallic fracture (green arrow in (a)). (c) Elongation and rotation of an initially present void (red arrow in (a)). (For interpretation of the references to color in this figure legend, the reader is referred to the web version of this article.)

while 38 new voids are formed between steps ⑤ and ⑥. These voids are primarily located inside intermetallic particles as shown exemplary in Fig. 11b. Similar to the one shown in Fig. 10b, fracture in the intermetallic particle occurs at an early stage of the loading process (here at ④-790N) and a second void has formed at the last step before failure ⑥. After final fracture ⑦, a total expanse of the two new voids of 2.8μm and 4.5μm in their width direction is measured. Fig. 11c tracks a single void in the deformation field as denoted by a red arrow in Fig 11a. Similar to the void in Fig. 10c, it elongates and rotates upon loading as quantified in Fig. 10d. The elongation rate increases only slowly at the beginning, but is accelerated significantly towards the last step before fracture and on the broken sample. At the same time, the void volume remains constant around 106μm^3 until the last step ⑦, where it slightly drops to 102μm^3.

The same methodology for separating pre-existing and newly created voids is applied to the whole gauge section sub-divided into three large regions (Fig. 5: “Left”, “Center”, “Right”). Fig. 12 shows the evolution of the two void populations for the three large regions by means of number of voids and corresponding void volume fraction. The number of new voids rises during step ② to more than 1500 in each region, which is attributed to early fracture but also laminography and thresholding uncertainties. The number of new voids further increases by about 400 at step ③ and reaches 3160 in the right region and 3700 in the left and middle regions at step ⑥. On the broken step ⑦, which could only be recovered for the left region, the number of new voids reaches 11700, corresponding to a three-fold increase compared to the previous step. Concerning the pre-exisiting voids, at the onset of plasticity, there are about 26'000 in each region, a number that decreases

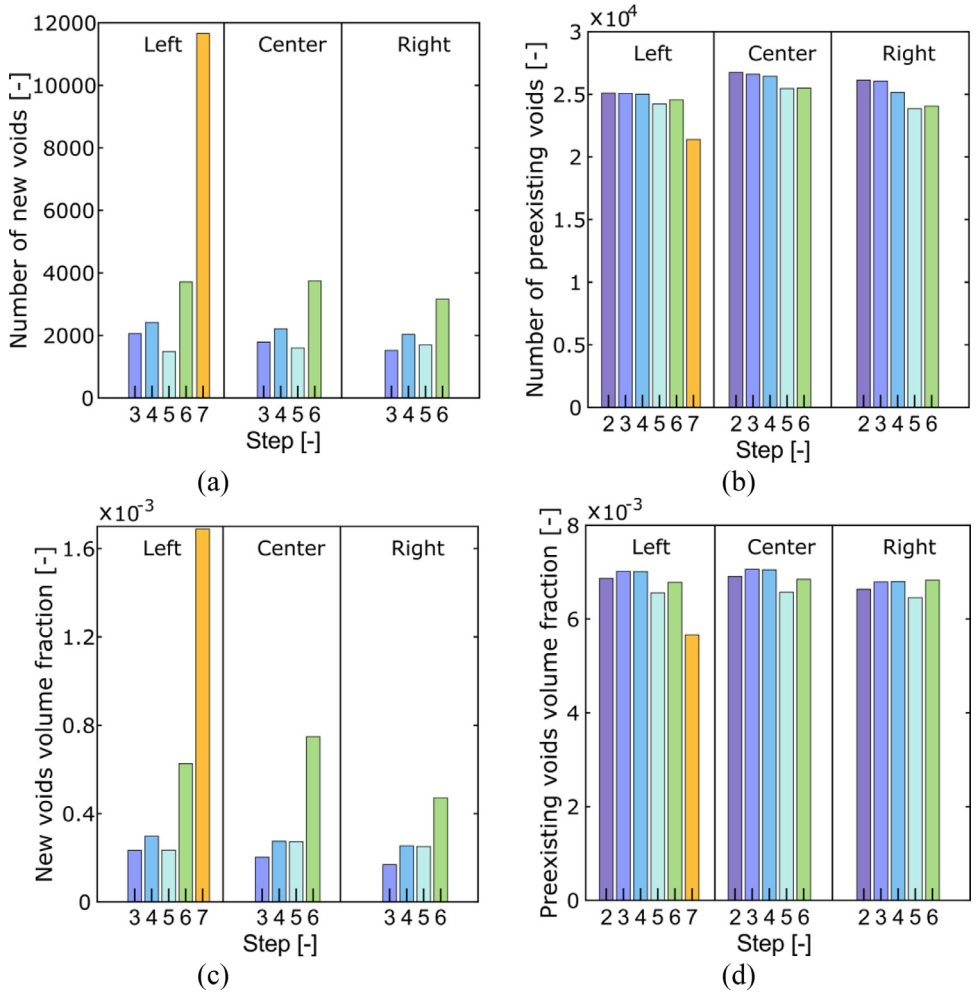

Fig. 12. Evolution of the pre-existing and new voids throughout the loading. The voids are tracked on the three large bins covering the gauge section (compare Fig. 5). (a) and (b) shows the evolution of the voids number while (c) and (d) shows the void volume fraction.

by 2%, 5% and 8% in the left, middle and right region, respectively at step ⑥ (920N). Counter-intuitively step ⑤ is characterized by a decrease in the number of both new and pre-existing voids, which is tentatively attributed to laminography uncertainties. Looking at the void volume fraction of the newly formed voids, an initial value of around 0.00027 at step ④ (790N) and ⑤ (865N) is measured, before it increases significantly to 0.00063, 0.00075 and 0.00047 for the left, middle and right gauge sections at the last step before fracture ⑥. This corresponds to an increase by a factor of two to three. Regarding the preexisting voids, the initial void volume fraction is around 0.007 and remains around that value throughout the loading. As with the single void observed before (Fig. 11c), no significant volume change is observed until fracture. In this step (⑦) the void volume fraction drops by approximately 20% to 0.00566 which is attributed to void closing during the localization process and elastic unloading post fracture that may close voids to some extent and make them less observable by laminography. This void rotation and closure during simple shear is consistent with numerical findings using unit cell calculations [2,23,58]. To the best of the authors' knowledge, there has not been experimental proof on 3D data for this process in the literature.

Instead of the three large regions used above, in the following section the top, middle and bottom line (Fig. 5) are each subdivided into 15 equally spaced sub-regions. They are used to extract a line profile evolution throughout the loading history for the effective strain, the void count and individual volume as well as the void shape. Fig. 13 presents the line profile evolution for the 15 regions on the top line. The line profile of the effective strain (Fig. 13a) shows an increase during the loading history and localizes in the center of the gauge section between 400μm and 600μm. Clearly visible are the two deformation bands that appear with two maxima on the line. The horizontal location of the maxima does not evolve during loading and remains at 450μm and 520μm. Fig. 13b shows the void count for the 15 regions located on the top line, while the bar plot represents the line average.

A slight increase in the void count is measured upon loading from 1423 at step ② to 1535 at step ⑥, while upon failure ⑦ the void count decreases to 1477. As seen in Fig. 11a this increase is mostly related to the failure of intermetallic particles. Overall, there is only a negligible spatial dependency on the void count, with a maximum 8% higher than the average at around 340μm. Regarding the individual void volume evolution (Fig. 13d), the mean (resp. 9th decile) of the void volume remains fairly constant during the loading with a less than 2% increase. The marginal spatial evolution is attributed to the change in strain ratio from the left to the right flank of the specimen (see Fig. 9). However, the most important evolution can be seen when looking at evolution of the void shape (Fig. 13c). The Feret shape factor significantly decreases during the loading, with the exception of loading step ② (600N), in particular at a horizontal position between 400$\mu m$and 600μm. From step ③ (700N) to ⑥ (920N), the mean (resp. 9th decile) value decrease from 0.67 (resp. 0.39) to 0.6 (resp. 0.34). On

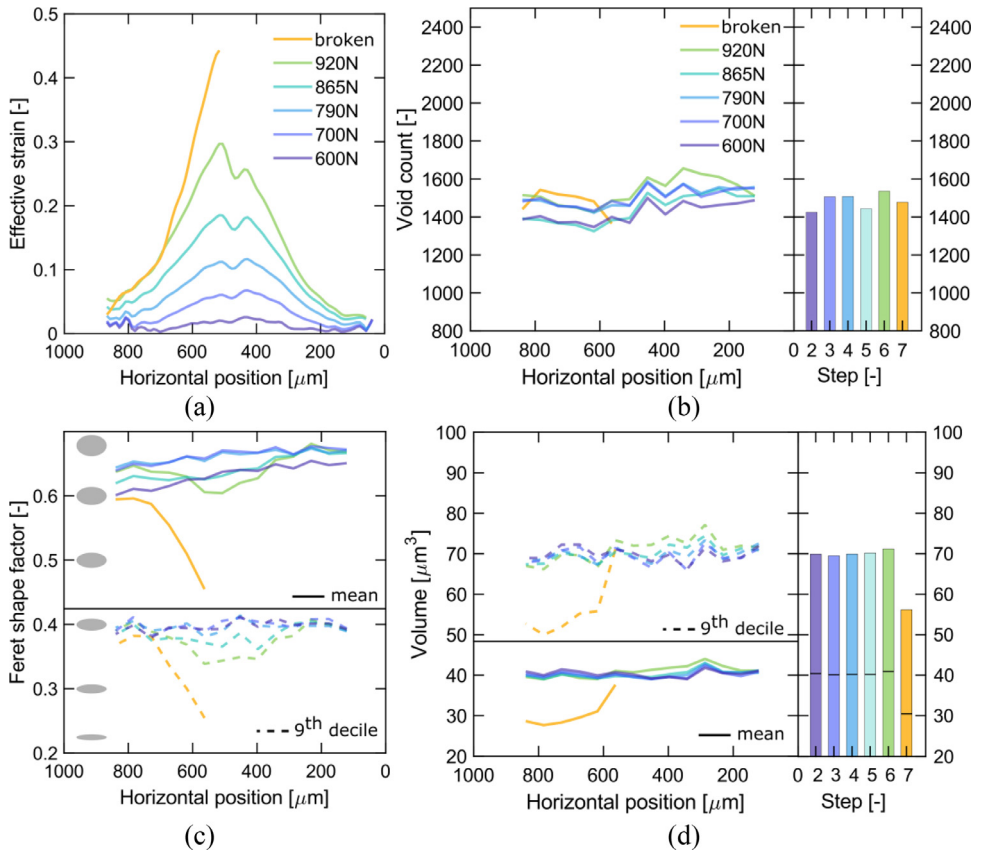

Fig. 13. Line profile evolution throughout the loading for 15 bins along the top line (compare Fig. 5). (a) Effective strain field from projection DIC, (b) void count obtained from laminography measurements, (c) Feret shape factor and (d) void volume.

the broken specimen ⑦, the decreasing trend is most severe, especially towards the center of the gauge section where the mean (resp. 9th decile) value reaches 0.45 (resp. 0.25). This means that for the least spherical ten percent of voids, the maximum principal axis length is four time larger than the minimum principal axis length. Similar conclusion can be drawn for the middle and bottom line.

The changes from the last step ⑥ to the broken sample ⑦ are attributed to two main factors: the deformation before fracture and the elastic unloading at the instant of fracture. While the change in void volume can be explained by the elastic unloading, the dramatic shape change is related to the strain localization in the material, as seen in Fig. 10 and 11 with the two-dimensional and three-dimensional representation of the voids.

3.4. Fractography

Fig. 14 shows SEM images of the fracture surface of the shear specimen post mortem. The fracture surface is characterized by elongated dimples aligned with the loading direction and large broken intermetallic particles, similar to the one seen in Fig. 11b. In Fig. 14a, a shattered intermetallic particle is shown that exhibits multiple cracks oriented normal to the loading direction. Similarly, in Fig. 14b a broken intermetallic particle is shown. The initial particle is cracked into three sub-particles with a distance of 2.4μm between the lower two and 3.5μm between the lower and the top part. Around this broken particle as well as on its left and right, grooves can be seen which extend by up to $3 \times 12 \mu m$. These grooves expose scale-shaped “drag marks” that are evidence that the particles play a significant role in the fracture process. It is speculated that the grooves observed below and above the three intermetallic particle fragments in Fig. 14b have been formed by particle motion and de-cohesion during the loading step before final fracture. At even smaller scale (Fig. 14c), ductile dimples seem to have initiated close to very small precipitates, i.e. dispersoids with an approximate size of 150nm. The dimples’ width is up to 1μm and up to a few micrometers in length.

4. Discussion

Before an in-depth discussion of the observed fracture mechanism and its chronology is carried out, the results of the numerical simulation of the shear specimen are discussed. This is necessary in an attempt to better understand the actual stress state during the test, which would not be obtainable solely from experimental results.

4.1. Comparison with finite element analysis

The numerically obtained force-displacement curve is presented in Fig. 7. The force level agrees very well with the experiment with a maximum error of only 20N at the onset of plasticity (②). In addition, the maximum effective strain along the top, bottom and middle lines is reported. For the top and bottom lines, close agreement is obtained, while towards the last step (⑥) the maximum effective strain along the middle line is significantly lower than the one obtained from DIC. Here, the simulation does not capture the rapid increase in the strain observed in the middle of the gauge section and the predicted effective strain is 0.22 while the experimentally measured value is 0.25, corresponding to a 13% discrepancy. However, the difference for the top and bottom line is less than 1%, from a measured average of 0.308 to the predicted value

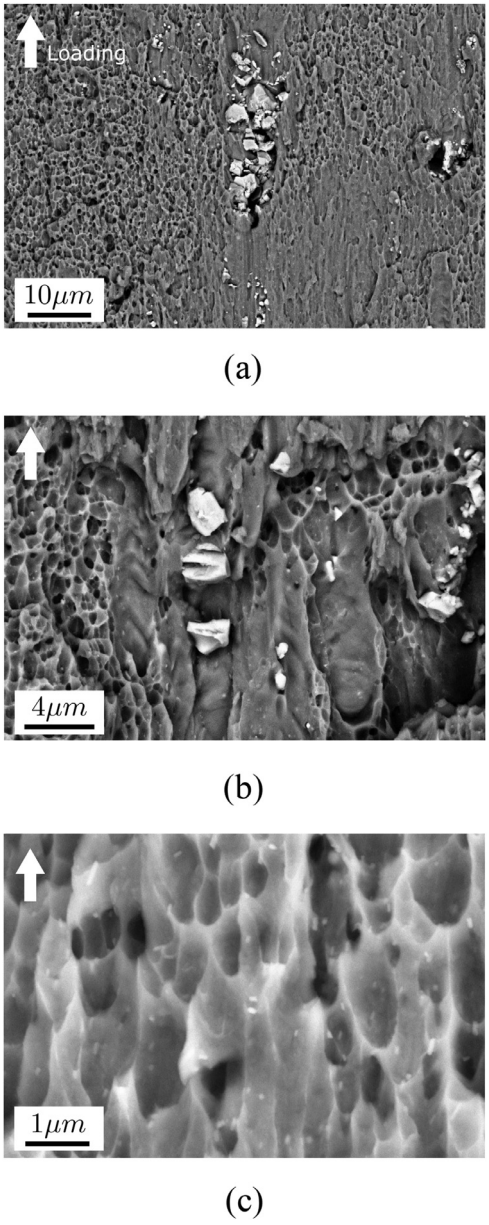

Fig. 14. Back-scattered electron images of the fracture surface at three different scales. (a) Overview of the fracture surface topography with small dimples and large broken intermetallic particles. (b) Fracture of an intermetallic particle normal to the loading direction. (c) Dimples and dispersoids located on the fracture surface.

of 0.306, as seen in Fig. 15a, where the effective strain is much more localized than on Fig. 8.

The stress state of the elements on the mid-plane of the shear specimen's gauge section at step ⑥ are shown by the solid dots in Fig. 6a. A slight deviation from the shear plane (grey dashed line SH) towards uniaxial tension plane (grey dashed line UT) is observed. This behavior is attributed to the material's anisotropy, what is also supported by the contour plots of the gauge section's mid-plane at the same step (Fig. 15b-c). When looking at the stress triaxiality field (Fig. 15b), a homogenous distribution with stress triaxialities between 0 and 0.1 in the central section is observed. This slightly deviates from a simple shear stress state towards tension. Additionally, two small regions of even stress triaxialities higher than 0.2 form towards the tensile loading arms on the bottom left and top right of the specimen. When looking at the distribution of the direction of the maximum principal stress

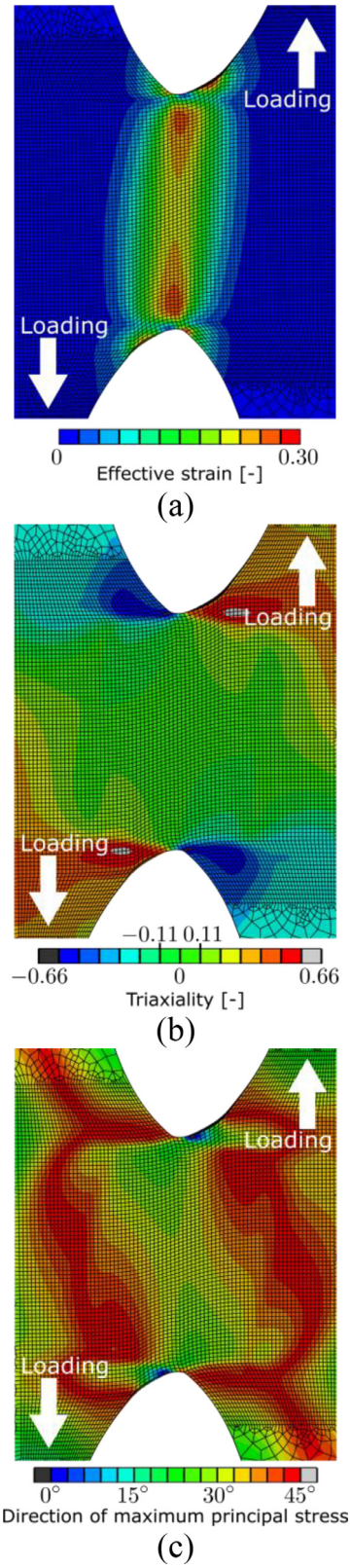

Fig. 15. Finite element results showing contour plots of (a) the effective strain, (b) the stress triaxiality and (c) the direction of the maximum principal stress with respect to the horizontal axis. The direction of the maximum principal stress lies between 26°and 32° in the gauge section with increasing width towards the tensile region.

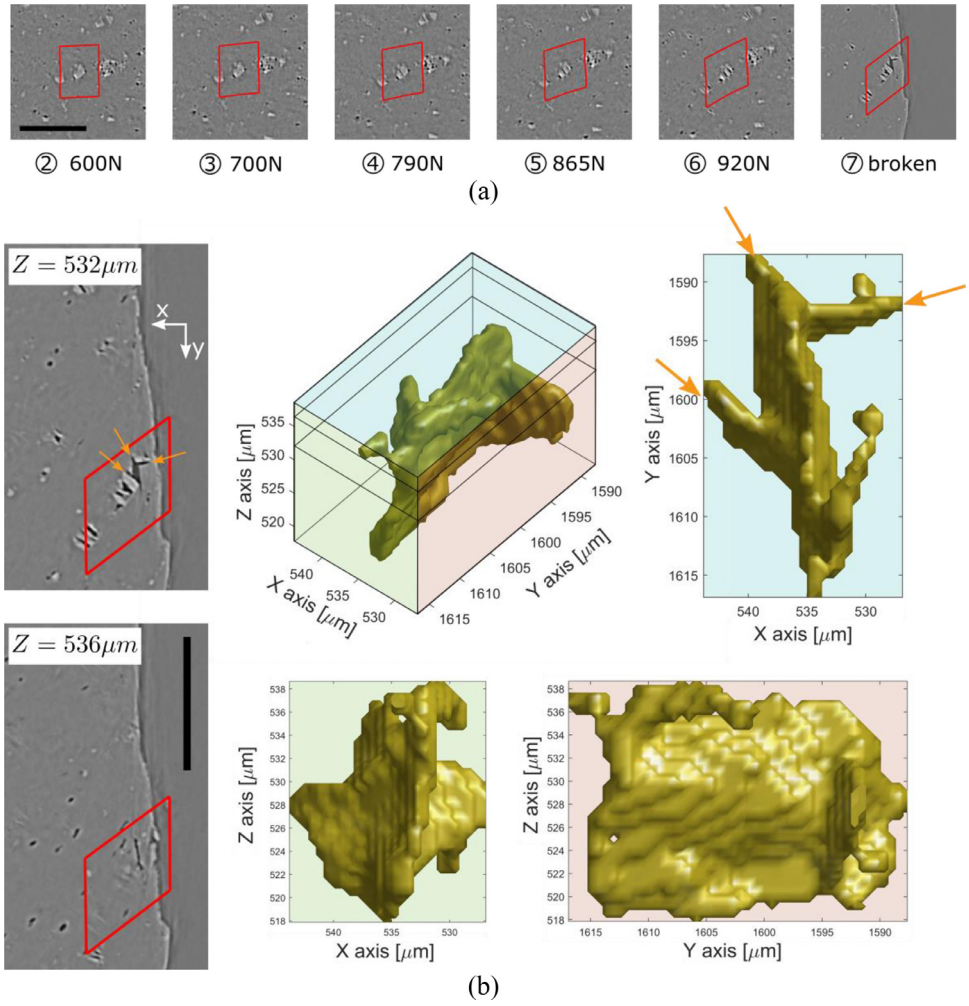

Fig. 16. Crack mechanism as observed around an intermetallic. (a) Evolution of the intermetallic on slice 534μm with loading. (b) Final laminography and 3D reconstruction view of a crack formed at the tip of an intermetallic. Orange arrows denote the location in the laminography and the 3D reconstruction. Both scale bars represent 100μm. (For interpretation of the references to color in this figure legend, the reader is referred to the web version of this article.)

(Fig. 15c), this becomes even more apparent. Instead of 45° as expected for simple shear, the direction of the maximum principal stress lies between 26°and 32° in the gauge section. This again supports the experimentally measured angle of 34° for the intermetallic particle cracking and fracture in Fig. 10b.

4.2. Fracture mechanism

Based on the experimental observations, the timeline from damage initiation to final fracture for the examined AA2024-T3 can now be based on the evolution of the two main features of the microstructure observed in the laminography experiments: intermetallic particles and pre-existing voids. Fig. 16a highlights the chronology leading to catastrophic failure, which is depicted in Fig.16b.

Between steps ② and ④: Early into the plastic loading, at low effective strain levels of the matrix material of less than 0.1, the strong but brittle intermetallic particles break for a first time normal to the direction of principal stress. (Figs. 16a, 10b, 11b). It should be emphasized that this is almost perpendicular to the direction of maximum principal strain and at 45° to the orientation of the final crack. At the same time, the pre-existing porosities follow the matrix material deformation (and rotation) with no noticeable change in volume.

Between steps ④ and ⑥: The intermetallic particles continue to break, fragmenting multiple times normal to the direction of principal stress, while the previously formed gaps grow with the change in the matrix strain field. The orientation of the gaps in conjunction with the strain field should induce shrinkage normal to the maximum principal strain and extension along that axis. However, void contraction is impeded by the debris of the fragmented particles leading to void growth. At the same time de-cohesion between the particle and the matrix is observed (Figs. 16a, 10b, 11b). The deformation of pre-existing voids continues to be primarily dictated by the rotation of the matrix and is not prone to any sudden event, even under large deformations.

Between steps ⑥ and ⑦: Due to the limited time resolution of the laminography technique and the very abrupt occurrence of final fracture, the following observations could only be made post mortem on the broken side of the specimen. While their existence is certain, the order of occurrence can only be speculated upon:

Formation of micro-cracks (Fig. 16b): The voids between the fragmented particles continue to grow. At this stage, smaller particle debris seems to be able to move freely leading to wider gap opening (Fig. 16b top and right arrow). The larger particle fragments are confined by the motion of the matrix material (Fig. 16b left arrow), resulting in stress concentrations around them. Subsequently micro-cracks form. For example the void closest to the fracture surface (Fig. 16b) grows substantially and rotates to almost align with the fracture plane, causing local softening. The initial void location is highlighted by the left arrow and is parallel to the other brittle cracks. The slice shown below is extracted 4μm above

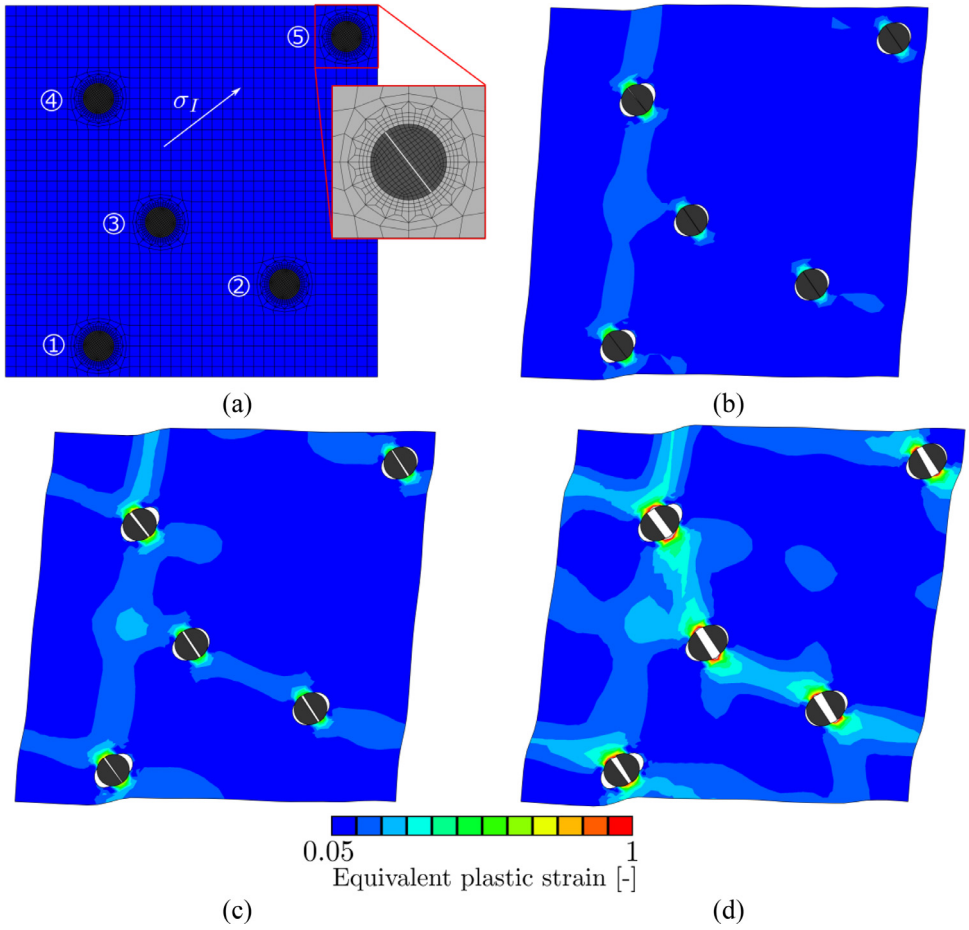

Fig. 17. RVE simulation including broken second-phase particles. (a) Initial RVE with mesh and orientation of the maximum principal stress and particle cracks. (b) Early deformation stage showing a vertical localization band as well as the decohesion between the particle and the matrix. (c) Competition between multiple bands and opening of the cracks. (d) Localization of the deformation in a path connecting the particles with the biggest void opening.

the crack main plane. At this height the void appears as a 20μm long crack aligned with the fracture plane. The three-dimensional views of the crack give more insight into the fracture mechanism. The large extension of the void on the broken sample appears to be a sudden event, not only related to the matrix deformation kinematics but rather to the accommodation of the local stress field variations induced by the failure of the intermetallic particle.

Formation of strain localization band (Fig. 10c, 11c). This feature's existence can only be proven experimentally by the change in the shape and size of the pre-existing voids from step ⑥ to ⑦. Here, close to the location of the final crack (Fig. 10c, 11c), a significant rotation and straining is observed. This is also in agreement with the evolution of effective strain profile shown in Figs. 13a, A1, A2.

Final fracture: It is speculated that upon loss of load carrying capacity, the nucleation of dimples around dispersoids drives final material separation in a void-sheet type of failure (Fig. 14c).

The chain of events leading to fracture of AA2024-T3 under shear begins with the failure of the brittle intermetallic particles normal to the maximum principal stress direction. The stagnation of the particle fragments in the displacement field of the matrix induce a void growth mechanism which for simple shear cannot be explained through basic micromechanical considerations due to the absence of a hydrostatic driving force. This fracture mechanism bears similarities with the shear fracture mechanism of FB600 steel presented in [42], where de-cohesion at the interface between the CaO-particles and the matrix leads to void growth and micro crack formation. It is worth noting that Tekoglu et al. [59] showed numerically that macroscopic localization precedes coalescence for stress triaxiality values larger than 1, while mentioning that this threshold might be too high for randomly distributed voids. Here this temporal order is shown experimentally at a stress triaxiality of around 0.1.

To shed more light on the fracture mechanisms, a representative volume element (RVE) simulation is conducted following the procedure defined in [42]. The microstructure is simplified to a matrix containing only spherical hard particles representing the intermetallic particles. The RVE is filled with 5 randomly-positioned particles corresponding to an area fraction of 2.7%. No attempt is made at simulating the brittle failure of the particles, hence the simulation starts with a plastic pre-strain of 5%. To represent the experimental observation, an initial crack is introduced in the middle of the particles. The crack is initially oriented normal to the direction of the applied maximum principal stress. The interaction between the particles and the matrix are defined using a penalty contact with a friction coefficient of 0.05 and no-separation condition. Between the two halves of the broken particles, the simple penalty contact is assumed with the same friction coefficient. The intermetallic particles are assumed to be isotropic and linear elastic with a Young's modulus of 140GPa and a Poisson's ratio of 0.33. The matrix is assumed to be isotropic elasto-plastic with a von Mises yield surface and the same hardening law as described in Section 2.2.3, thereby effectively removing any effect of the matrix anisotropy on the localization. The loading is applied through periodic boundary conditions enforcing the triaxiality to be 0.1 and the maximum principal stress direction to be oriented at 37.5° with

respect to the horizontal axis (white line in Fig. 17a). The region surrounding the particles is meshed with an element size corresponding to 1/8 of the particle radius while a larger mesh is used in the matrix leading to a total element number of 3536.

The results are depicted in Fig. 17. At an early stage of loading, the particles detach from the matrix and two cavities form aligned with the direction of principal stress, while no opening of the particles is observed. The deformation localizes into a vertical band from particles ① to ④. The opening of the particles is only observed at a later stage of loading where the deformation localizes in multiple bands, thus linking the particles. Finally, the localization occurs between particles ②, ③ and ④ showing large particle cracking normal to the direction of maximum principal stress. Particles ① and ⑤ exhibit rotation of the cavity inside the particles similar to the one observed on the broken sample on Fig. 16a.

In the present study, in-situ X-ray synchrotron laminography is used to observe the failure mechanism of a 2024-T3 aluminum alloy under shear-dominated loading. Six loading steps as well as the fully-fractured specimen are analyzed. A high spatial resolution with a voxel size of $0.65\mu m$ is chosen to observe the evolution of intermetallic particles and porosities. The material features a high initial volume fraction of preexisting voids in the matrix (around 0.7%). These voids are used as markers for through-thickness projection DIC. A homogeneous strain field is observed in the highly stretched regions, with an effective strain of 0.3 in the last step prior to failure. Projection DIC is also used to represent the voids back in the reference configuration and separate preexisting from nucleated voids. To the best of the authors' knowledge, this is the first time that both classes of voids can be separated, allowing statistics related to both populations to be generated. Feret's shape factor and the volume of individual voids are monitored during the loading. Consistent with the kinematics of simple shear, an almost constant void volume is observed throughout the experiments along with a strong elongation and flattening of the voids. For the tested aluminum 2024-T3, the evolution of the void volume fraction is quantified in detail. It shows a significant growth of (newly-) nucleated voids towards the end of the tests. This information will be beneficial for the calibration of advanced porous plasticity and fracture models (e.g. [60]).

Besides the global statistics, an in-depth analysis of the damage mechanisms leading to final fracture is carried out. It is found that preexisting voids deform by rotating, elongating and closing, thereby strictly following the homogenized strain field as measured by projection DIC. Intermetallic particles fail in a two-stage manner. At low strain levels, a first crack forms inside the particles normal to the direction of the maximum principal stress. These nucleated voids open up during loading, thereby leading to large cavities. Due to the abrupt failure, it is not possible to observe the exact instant of fracture with laminography. However, post-mortem fractography reveals that the broken intermetallic particles are subjected to large rigid-body motions upon failure. Away from the intermetallic particles, the fracture surface is covered by small ductile dimples containing dispersoids. In addition to experiments, an RVE simulation with periodic boundary conditions is performed to model the failure mechanism of the intermetallic particles. The simulation results show that opening of the pre-cracked particles leads to high strain concentrations at the mesoscopic level that ultimately results in strain bands linking the particles.

Declaration of Competing Interest

The authors declare that they have no known competing financial interests or personal relationships that could have appeared to influence the work reported in this paper.

Acknowledgements

The authors would like to thank Dr. Henry Proudhon (Mines ParisTech) and Prof. Vincent Grolleau (Université Bretagne Sud/ETH) for fruitful discussions. Dr. Ante Buljac and Xiang Kong (Mines ParisTech) are thanked for the help with the scanning and post-processing. The ANR is thanked for partial funding of this work (projects: Cominside ANR-14-CE07-0034 and LAMBDA ANR-17-CE08-0051). The ESRF is thanked for providing beamtime during the experiment mi1241.

References

[1] A. Pineau, A.A. Benzerga, T. Pardoen, Failure of metals I: brittle and ductile fracture, Acta Mater. 107 (2016) 424–483, doi:10.1016/j.actamat.2015.12.034.
[2] F.A. McClintock, A criterion for ductile fracture by the growth of holes, J. Appl. Mech. 35 (1968) 363–371, doi:10.1115/1.3601204.
[3] J.R. Rice, D.M. Tracey, On the ductile enlargement of voids in triaxial stress fields*, J. Mech. Phys. Solids. 17 (1969) 201–217, doi:10.1016/0022-5096(69)90033-7.
[4] I. Barsoum, J. Faleskog, Rupture mechanisms in combined tension and shear-micromechanics, Int. J. Solids Struct. 44 (2007) 5481–5498, doi:10.1016/j.ijsolstr.2007.01.010.
[5] K. Nahshon, J.W. Hutchinson, Modification of the gurson model for shear failure, Eur. J. Mech. - A/Solids. 27 (2008) 1–17, doi:10.1016/j.euromechsol.2007.08.002.
[6] T. Wierzbicki, L. Xue, On the effect of the third invariant of the stress deviator on ductile fracture, Impact Crashworthiness Lab. Tech. Rep. 136 (2005).
[7] Y. Bai, T. Wierzbicki, A new model of metal plasticity and fracture with pressure and lode dependence, Int. J. Plast. 24 (2008) 1071–1096, doi:10.1016/j.ijplas.2007.09.004.
[8] M. Brünig, O. Chyra, D. Albrecht, L. Driemeier, M. Alves, A ductile damage criterion at various stress triaxialities, Int. J. Plast. 24 (2008) 1731–1755, doi:10.1016/j.ijplas.2007.12.001.
[9] Y. Lou, H. Huh, S. Lim, K. Pack, New ductile fracture criterion for prediction of fracture forming limit diagrams of sheet metals, Int. J. Solids Struct. 49 (2012) 3605–3615, doi:10.1016/j.ijsolstr.2012.02.016.
[10] D. Mohr, S.J. Marcadet, Micromechanically-motivated phenomenological Hosford-Coulomb model for predicting ductile fracture initiation at low stress triaxialities, Int. J. Solids Struct. 67–68 (2015) 40–55, doi:10.1016/j.ijsolstr.2015.02.024.
[11] K. Danas, P.P. Castañeda, Influence of the Lode parameter and the stress triaxiality on the failure of elasto-plastic porous materials, Int. J. Solids Struct. 49 (2012) 1325–1342, doi:10.1016/j.ijsolstr.2012.02.006.
[12] M. Gologanu, J.-B. Leblond, J. Devaux, Approximate models for ductile metals containing non-spherical voids—case of axisymmetric prolate ellipsoidal cavities, J. Mech. Phys. Solids. 41 (1993) 1723–1754, doi:10.1016/0022-5096(93)90029-F.
[13] K. Madou, J.-B. Leblond, A Gurson-type criterion for porous ductile solids containing arbitrary ellipsoidal voids—I: limit-analysis of some representative cell, J. Mech. Phys. Solids. 60 (2012) 1020–1036, doi:10.1016/j.jmps.2011.11.008.
[14] K. Madou, J.-B. Leblond, A Gurson-type criterion for porous ductile solids containing arbitrary ellipsoidal voids—II: determination of yield criterion parameters, J. Mech. Phys. Solids. 60 (2012) 1037–1058, doi:10.1016/j.jmps.2012.01.010.
[15] T.F. Morgeneyer, J. Besson, Flat to slant ductile fracture transition: Tomography examination and simulations using shear-controlled void nucleation, Scr. Mater. 65 (2011) 1002–1005, doi:10.1016/j.scriptamat.2011.09.004.
[16] A.S. Argon, Formation of cavities from nondeformable second-phase particles in low temperature ductile fracture, J. Eng. Mater. Technol. 98 (1976) 60–68, doi:10.1115/1.3443338.
[17] L.E. Bryhni Dæhli, T. Børvik, O.S. Hopperstad, Influence of loading path on ductile fracture of tensile specimens made from aluminium alloys, Int. J. Solids Struct. 88–89 (2016) 17–34, doi:10.1016/j.ijsolstr.2016.03.028.
[18] A. Ghahremaninezhad, K. Ravi-Chandar, Ductile failure behavior of polycrystalline Al 6061-T6, Int. J. Fract. 174 (2012) 177–202. 10.1007/s10704-012-9689-z.
[19] D. Steglich, W. Brocks, Micromechanical modelling of the behaviour of ductile materials including particles, Comput. Mater. Sci. 9 (1997) 7–17, doi:10.1016/S0927-0256(97)00053-0.
[20] N.A. Fleck, J.W. Hutchinson, V. Tvergaard, Softening by void nucleation and growth in tension and shear, J. Mech. Phys. Solids. 37 (1989) 515–540, doi:10.1016/0022-5096(89)90027-6.
[21] M.E. Torki, C. Tekoğlu, J.-B. Leblond, A.A. Benzerga, Theoretical and numerical analysis of void coalescence in porous ductile solids under arbitrary loadings, Int. J. Plast. 91 (2017) 160–181, doi:10.1016/j.ijplas.2017.02.011.
[22] K.L. Nielsen, J. Dahl, V. Tvergaard, Collapse and coalescence of spherical voids subject to intense shearing: studied in full 3D, Int. J. Fract. 177 (2012) 97–108, doi:10.1007/s10704-012-9757-4.
[23] M. Dunand, D. Mohr, Effect of Lode parameter on plastic flow localization after proportional loading at low stress triaxialities, J. Mech. Phys. Solids. 66 (2014) 133–153, doi:10.1016/J.JMPS.2014.01.008.
[24] L. Morin, J.-B. Leblond, D. Mohr, D. Kondo, Prediction of shear-dominated ductile fracture in a butterfly specimen using a model of plastic porous solids

including void shape effects, Eur. J. Mech. - A/Solids. 61 (2017) 433–442, doi:10.1016/j.euromechsol.2016.10.014.
[25] Y. Bao, T. Wierzbicki, On fracture locus in the equivalent strain and stress triaxiality space, Int. J. Mech. Sci. (2004), doi:10.1016/j.ijmecsci.2004.02.006.
[26] D. Mohr, S. Henn, Calibration of stress-triaxiality dependent crack formation criteria: a new hybrid experimental?numerical method, Exp. Mech. 47 (2007) 805–820, doi:10.1007/s11340-007-9039-7.
[27] S. Gerke, P. Adulyasak, M. Brünig, New biaxially loaded specimens for the analysis of damage and fracture in sheet metals, Int. J. Solids Struct. 110–111 (2017) 209–218, doi:10.1016/j.ijsolstr.2017.01.027.
[28] J. Papasidero, V. Doquet, D. Mohr, Ductile fracture of aluminum 2024-T351 under proportional and non-proportional multi-axial loading: Bao â€"Wierzbicki results revisited, Int. J. Solids Struct. 69–70 (2015) 459–474, doi:10.1016/j.ijsolstr.2015.05.006.
[29] C.C. Roth, D. Mohr, Ductile fracture experiments with locally proportional loading histories, Int. J. Plast. 79 (2016) 328–354, doi:10.1016/j.ijplas.2015.08.004.
[30] M. Dunand, D. Mohr, Optimized butterfly specimen for the fracture testing of sheet materials under combined normal and shear loading, Eng. Fract. Mech. 78 (2011) 2919–2934, doi:10.1016/j.engfracmech.2011.08.008.
[31] J. Peirs, P. Verleysen, W. Van Paepegem, J. Degrieck, Determining the stress-strain behaviour at large strains from high strain rate tensile and shear experiments, Int. J. Impact Eng. 38 (2011) 406–415, doi:10.1016/j.ijimpeng.2011.01.004.
[32] V. Tarigopula, O.S. Hopperstad, M. Langseth, A.H. Clausen, F. Hild, O.G. Lademo, M. Eriksson, A study of large plastic deformations in dual phase steel using digital image correlation and FE analysis, Exp. Mech. (2008), doi:10.1007/s11340-007-9066-4.
[33] D. Mohr, R. Treitler, Onset of fracture in high pressure die casting aluminum alloys, Eng. Fract. Mech. 75 (2008) 97–116, doi:10.1016/j.engfracmech.2007.01.029.
[34] A.J. Gross, K. Ravi-Chandar, On the deformation and failure of Al 6061-T6 at low triaxiality evaluated through in situ microscopy, Int. J. Fract. 200 (2016) 185–208, doi:10.1007/s10704-016-0078-x.
[35] J. Papasidero, V. Doquet, D. Mohr, Determination of the effect of stress state on the onset of ductile fracture through tension-torsion experiments, Exp. Mech. 54 (2014) 137–151, doi:10.1007/s11340-013-9788-4.
[36] B.P. FLANNERY, H.W. DECKMAN, W.G. ROBERGE, K.L. DAMICO, Three-dimensional X-ray microtomography, Science (80-.). 237 (1987) 1439 LP – 1444, doi:10.1126/science.237.4821.1439.
[37] A. King, G. Johnson, D. Engelberg, W. Ludwig, J. Marrow, Observations of intergranular stress corrosion cracking in a grain-mapped polycrystal, Science (80-.) 321 (2008) 382 LP – 385, doi:10.1126/science.1156211.
[38] E. Maire, P.J. Withers, Quantitative X-ray tomography, Int. Mater. Rev. 59 (2014) 1–43, doi:10.1179/1743280413Y.0000000023.
[39] T.F. Morgeneyer, L. Helfen, I. Sinclair, H. Proudhon, F. Xu, T. Baumbach, Ductile crack initiation and propagation assessed via in situ synchrotron radiation-computed laminography, Scr. Mater. 65 (2011) 1010–1013, doi:10.1016/j.scriptamat.2011.09.005.
[40] L. Helfen, A. Myagotin, P. Mikulík, P. Pernot, A. Voropaev, M. Elyyan, M. Di Michiel, J. Baruchel, T. Baumbach, On the implementation of computed laminography using synchrotron radiation, Rev. Sci. Instrum. 82 (2011) 63702, doi:10.1063/1.3596566.
[41] T. Ueda, L. Helfen, T.F. Morgeneyer, In situ laminography study of three-dimensional individual void shape evolution at crack initiation and comparison with Gurson–Tvergaard–Needleman-type simulations, Acta Mater 78 (2014) 254–270, doi:10.1016/j.actamat.2014.06.029.
[42] C.C. Roth, T.F. Morgeneyer, Y. Cheng, L. Helfen, D. Mohr, Ductile damage mechanism under shear-dominated loading: In-situ tomography experiments on dual phase steel and localization analysis, Int. J. Plast. (2018), doi:10.1016/j.ijplas.2018.06.003.
[43] A. Buljac, F. Hild, L. Helfen, T.F. Morgeneyer, On deformation and damage micromechanisms in strong work hardening 2198 T3 aluminium alloy, Acta Mater. 149 (2018) 29–45, doi:10.1016/j.actamat.2018.01.026.
[44] R.P. Walker, Insertion devices: undulators and wigglers, in: Cern Accel. Sch. Course Synchrotron Radiat. Free, Lasers, 1996, pp. 129–190.
[45] L. Helfen, A. Myagotin, A. Rack, P. Pernot, P. Mikulík, M. Di Michiel, T. Baumbach, Synchrotron-radiation computed laminography for high-resolution three-dimensional imaging of flat devices, Phys. Status Solidi. 204 (2007) 2760–2765, doi:10.1002/pssa.200775676.
[46] A. Myagotin, A. Voropaev, L. Helfen, D. Hänschke, T. Baumbach, Efficient volume reconstruction for parallel-beam computed laminography by filtered backprojection on multi-core clusters, IEEE Trans. Image Process. 22 (2013) 5348–5361, doi:10.1109/TIP.2013.2285600.
[47] M. Vogelgesang, T. Farago, T.F. Morgeneyer, L. Helfen, T. dos Santos Rolo, A. Myagotin, T. Baumbach, Real-time image-content-based beamline control for smart 4D X-ray imaging, J. Synchrotron Radiat. 23 (2016) 1254–1263, doi:10.1107/S1600577516010195.
[48] A. Buljac, L. Helfen, F. Hild, T.F. Morgeneyer, Effect of void arrangement on ductile damage mechanisms in nodular graphite cast iron: In situ 3D measurements, Eng. Fract. Mech. 192 (2018) 242–261, doi:10.1016/j.engfracmech.2018.01.008.
[49] V.M. Trejo Navas, A. Buljac, F. Hild, T. Morgeneyer, L. Helfen, M. Bernacki, P.-O. Bouchard, A comparative study of image segmentation methods for micromechanical simulations of ductile damage, Comput. Mater. Sci. 159 (2019) 43–65, doi:10.1016/j.commatsci.2018.11.039.
[50] E.P. Denis, C. Barat, D. Jeulin, C. Ducottet, 3D complex shape characterization by statistical analysis: application to aluminium alloys, Mater. Charact. 59 (2008) 338–343, doi:10.1016/j.matchar.2007.01.012.
[51] F. Barlat, J.C. Brem, J.W. Yoon, K. Chung, R.E. Dick, D.J. Lege, F. Pourboghrat, S.-H. Choi, E. Chu, Plane stress yield function for aluminum alloy sheets—part 1: theory, Int. J. Plast. 19 (2003) 1297–1319, doi:10.1016/S0749-6419(02)00019-0.
[52] M. Dunand, A.P. Maertens, M. Luo, D. Mohr, Experiments and modeling of anisotropic aluminum extrusions under multi-axial loading – Part I: plasticity, Int. J. Plast. 36 (2012) 34–49, doi:10.1016/j.ijplas.2012.03.003.
[53] M.B. Gorji, D. Mohr, Predicting shear fracture of aluminum 6016-T4 during deep drawing: combining Yld-2000 plasticity with Hosford–Coulomb fracture model, Int. J. Mech. Sci. 137 (2018) 105–120, doi:10.1016/j.ijmecsci.2018.01.008.
[54] V. Grolleau, C.C. Roth, V. Lafilé, B. Galpin, D. Mohr, Loading of mini-Nakazima specimens with a dihedral punch: determining the strain to fracture for plane strain tension through stretch-bending, Int. J. Mech. Sci. 152 (2019) 329–345, doi:10.1016/j.ijmecsci.2019.01.005.
[55] H.W. Swift, Plastic instability under plane stress, J. Mech. Phys. Solids. 1 (1952) 1–18., doi:10.1016/0022-5096(52)90002-1.
[56] E. Voce, The Relationship Between Stress and Strain for Homogeneous Deformations, 1948.
[57] C.C. Roth, D. Mohr, Determining the strain to fracture for simple shear for a wide range of sheet metals, Int. J. Mech. Sci. 149 (2018) 224–240, doi:10.1016/j.ijmecsci.2018.10.007.
[58] V. Tvergaard, Study of localization in a void-sheet under stress states near pure shear, Int. J. Solids Struct. 75–76 (2015) 134–142, doi:10.1016/j.ijsolstr.2015.08.008.
[59] C. Tekoılu, J.W. Hutchinson, T. Pardoen, On localization and void coalescence as a precursor to ductile fracture, Philos. Trans. R. Soc. A Math. Phys. Eng. Sci. (2015) 373, doi:10.1098/rsta.2014.0121.
[60] N. Pathak, J. Adrien, C. Butcher, E. Maire, M. Worswick, Experimental stress state-dependent void nucleation behavior for advanced high strength steels, Int. J. Mech. Sci. 179 (2020) 105661, doi:10.1016/j.ijmecsci.2020.105661.